Machine-learning accelerated density-explicit polymer field theory simulations

Duyu Chen,[1] Yao Xuan,[2] Hector D. Ceniceros,[2] and Glenn H. Fredrickson[1,3]

[1)]*Materials Research Laboratory, University of California, Santa Barbara, California 93106, USA*

[2)]*Department of Mathematics, University of California, Santa Barbara, California 93106, USA*

[3)]*Department of Chemical Engineering, University of California, Santa Barbara, California 93106, United States*

(*Electronic mail: ghf@mrl.ucsb.edu)

(*Electronic mail: duyu@alumni.princeton.edu)

(Dated: 13 August 2025)

Recently, the density-explicit framework that describes thermodynamic properties of multicomplonent polymer systems as functionals of both auxiliary and density fields has attracted growing interest for simulations in polymer field theory. This is due to the flexibility of the framework in accommodating various forms of intermolecular potentials, and in particular, the easy generalization to many-body interactions beyond pair potentials. However, numerical simulations based on the formalism are generally more expensive due to the increased number of fields, compared to the conventional auxiliary field framework. A commonly used simplification in the density-explicit setting is the partial saddle point approximation, where functional integrals over the species auxiliary fields are replaced by the value of the integrand evaluated at the field configuration that makes the functional derivative of the Hamiltonian with respect to the species auxiliary fields vanish. These "partial saddle point" field configurations provide the dominant *mean-field* contribution to the field theory and facilitate estimation of polymer structure and thermodynamic properties.

In this work, we study analytically and numerically the solutions of partial saddle points of the species auxiliary fields for different representative density fields. This initial study inspires us to develop deep neural networks with efficient local and low-dimensional feature representations that are applicable across different spatial resolutions and dimensions. We train these neural networks on one-dimensional simulation data to accurately predict partial saddle points under different conditions. As a proof of concept, we find that our machine-learned models produce high-quality initial guesses for field configurations that considerably accelerate new simulations at resolutions far exceeding the training data resolution. Our results may serve as a stepping stone toward accurate and efficient prediction of the phase behavior of complex block copolymer mesophases, as well as a blueprint for developing machine learning-assisted field theoretic simulation tools for the computational study of polymers and soft matter systems more broadly.

I. INTRODUCTION

Computer simulations[1–4] based on polymer field theory[5] have been widely used to investigate the equilibrium phase behavior of heterogeneous polymers during the last few decades. Depending on the amount of fluctuations included, field theory studies can be further divided into three categories: self-consistent field theory (SCFT) simulations that are at the mean-field level and incorporate no fluctuations, random-phase approximation (RPA) studies that involve Gaussian fluctuations around homogeneous mean-field solutions, and fully fluctuating field-theoretic simulations (FTS) that take into account all fluctuations.[2,6] Most previous field theory studies have adopted the standard auxiliary-field (AF) framework,[1,2] in which Hubbard–Stratonovich transformations[7] are utilized to decouple non-bonded interactions among polymer chains and replace them with independent interactions between a single polymer chain and one or more auxiliary potential fields $w(\mathbf{r})$.[2] The AF framework, despite its popular use, requires that the pair potential $u(r)$ is positive or negative definite and possesses an inverse, so is difficult to generalize to many-body interactions beyond pairwise interactions.[2,8–10]

Recently, efforts have been devoted to develop simulation tools based on the hybrid density-explicit auxiliary field (DE-AF) framework.[10] In this alternative framing of polymer field theory, both species density fields $\rho(\mathbf{r})$ and auxiliary potential fields $w(\mathbf{r})$ are retained,[11]. This removes the pair potential constraint on the interaction potentials in the AF framework. Also, in the DE-AF framework, one has access to physical observables associated with instantaneous density fields, which enable simulations of non-equilibrium systems, e.g., in the context of dynamic self-consistent field theory (DSCFT).[11–16] Specifically, using the incompressible melt of a linear AB diblock copolymer with the continuous Gaussian chain model as an example, in this framework the canonical partition function $Z_C(n,V,T)$ is given by[10]

$$Z_C(n,V,T) = Z_0 \int D\phi \int Dw_A \int Dw_B \, e^{-H[\phi,w_A,w_B]}, \tag{1}$$

$$\begin{aligned} H[\phi,w_A,w_B] = C\Bigg\{ &\chi N \int d\mathbf{r}\, \phi(\mathbf{r})[1-\phi(\mathbf{r})] - \int d\mathbf{r}\, iw_A(\mathbf{r})\phi(\mathbf{r}) \\ &- \int d\mathbf{r}\, iw_B(\mathbf{r})[1-\phi(\mathbf{r})] - \bar{V}\ln Q[iw_A, iw_B] \Bigg\}, \end{aligned} \tag{2}$$

where Z_0 is the ideal gas contribution, n is the number of polymers, V is the volume, N is the polymer degree of polymerization, and $\rho_0 = nN/V$ is the average polymer segment density. Parameters in the model include the Flory–Huggins interaction parameter χ, the volume fraction

of type A segments $f = N_A/(N_A+N_B)$, the dimensionless chain concentration $C = nR_g^3/V$, the dimensionless volume $\bar{V} = V/R_g^3$, and the unperturbed polymer radius of gyration R_g (all lengths in the model are scaled by R_g). The field $\phi(\mathbf{r}) = \phi_A(\mathbf{r}) = \rho_A(\mathbf{r})/\rho_0$ is the species volume fraction or normalized density field of the A block, and $w_A(\mathbf{r})$ and $w_B(\mathbf{r})$ are the species auxiliary fields (normalized by N) of the A and B blocks, respectively. Note that due to the incompressible melt condition, the volume fraction field $\phi_B(\mathbf{r})$ of the B block is given by $\phi_B(\mathbf{r}) = 1-\phi(\mathbf{r})$. Here, the normalized partition function $Q[iw_A, iw_B]$ is given by

$$Q[iw_A, iw_B] = \frac{1}{\bar{V}}\int d\mathbf{r}\, q(\mathbf{r},1;[iw_A,iw_B]) = \frac{1}{\bar{V}}\int d\mathbf{r}\, q_c(\mathbf{r},1;[iw_A,iw_B]), \tag{3}$$

where the chain propagator $q(\mathbf{r},s;[iw_A,iw_B])$ satisfies the Fokker-Planck equation

$$\frac{\partial}{\partial s}q(\mathbf{r},s;[iw_A,iw_B]) = \nabla^2 q(\mathbf{r},s;[iw_A,iw_B]) - iw(\mathbf{r},s)q(\mathbf{r},s;[iw_A,iw_B]), \tag{4}$$

and is initialized from the A block end with the initial condition $q(\mathbf{r},0)=1$, and the corresponding auxiliary field $w(\mathbf{r},s)$ is given by

$$w(\mathbf{r},s) = \begin{cases} w_A(\mathbf{r}), & 0 \le s \le f, \\ w_B(\mathbf{r}), & f < s \le 1. \end{cases} \tag{5}$$

The complementary chain propagator $q_c(\mathbf{r},s;[iw_A,iw_B])$, on the other hand, propagates from the B block end with the initial condition $q_c(\mathbf{r},0)=1$, and satisfies the analogous diffusion equation

$$\frac{\partial}{\partial s}q_c(\mathbf{r},s;[iw_A,iw_B]) = \nabla^2 q_c(\mathbf{r},s;[iw_A,iw_B]) - iw_c(\mathbf{r},s)q_c(\mathbf{r},s;[iw_A,iw_B]), \tag{6}$$

where the corresponding auxiliary field $w_c(\mathbf{r},s)$ is given by

$$w_c(\mathbf{r},s) = \begin{cases} w_B(\mathbf{r}), & 0 \le s \le 1-f, \\ w_A(\mathbf{r}), & 1-f < s \le 1. \end{cases} \tag{7}$$

To evaluate the functional integrals with respect to the auxiliary fields $w_A(\mathbf{r})$ and $w_B(\mathbf{r})$ in the partition function, one can further invoke the partial saddle-point approximation (PSPA),[10] and replace the integrals with the leading (mean-field) contribution, i.e.,

$$\int Dw_A \int Dw_B e^{-H[\phi,w_A,w_B]} \approx e^{-H[\phi,w_A^*[\phi],w_B^*[\phi]]}, \tag{8}$$

$$\left.\frac{\delta H[\phi,w_A,w_B]}{\delta w_A(\mathbf{r})}\right|_{w_A^*[\phi],w_B^*[\phi]} = -iC\left\{\phi(\mathbf{r}) - \tilde{\phi}_A(\mathbf{r})\right\} = 0, \tag{9}$$

$$\left.\frac{\delta H[\phi,w_A,w_B]}{\delta w_B(\mathbf{r})}\right|_{w_A^*[\phi],w_B^*[\phi]} = -iC\left\{1-\phi(\mathbf{r})-\tilde{\phi}_B(\mathbf{r})\right\} = 0. \tag{10}$$

where the volume fraction operators $\tilde{\phi}_A(\mathbf{r})$ and $\tilde{\phi}_B(\mathbf{r})$ are given by

$$\tilde{\phi}_A(\mathbf{r}) = -\bar{V}\frac{\delta \ln Q}{\delta i w_A} = \frac{1}{Q[iw_A,iw_B]}\int_0^f ds\, q_c(\mathbf{r},1-s;[iw_A,iw_B])q(\mathbf{r},s;[iw_A,iw_B]), \tag{11}$$

and

$$\tilde{\phi}_B(\mathbf{r}) = -\bar{V}\frac{\delta \ln Q}{\delta i w_B} = \frac{1}{Q[iw_A,iw_B]}\int_f^1 ds\, q_c(\mathbf{r},1-s;[iw_A,iw_B])q(\mathbf{r},s;[iw_A,iw_B]). \tag{12}$$

Note that these equations governing the partial saddle points reveal that the mapping from $\phi(\mathbf{r})$ to $w_A(\mathbf{r})$ and $w_B(\mathbf{r})$ is inherently nonlinear and nonlocal for general density profiles $\phi(\mathbf{r})$.

Alternatively, one can also utilize complex Langevin (CL) dynamics[10] to sample the field states representative of the complex distribution $\exp(-H[\phi,w_A,w_B])$, which is a more accurate but also more computationally intensive way to evaluate the integrals with respect to $w_A(\mathbf{r})$ and $w_B(\mathbf{r})$. It is noteworthy that even with the PSPA, approximating these integrals is computationally expensive, given the cost to find the partial saddle points $w_A^*[\phi]$ and $w_B^*[\phi]$ in particular for instantaneous density fields $\phi(\mathbf{r})$ that are not saddle points of H. This is part of the reason why the development and application of simulation tools based on the DE-AF framework has been very limited, apart from the challenge to preserve the positivity of the density fields when sampling the functional integral with respect to $\phi(\mathbf{r})$.[10]

The rapid development of machine learning (ML) tools, in particular those based on deep neural networks in recent years presents transformative opportunities to enhance and accelerate polymer field theory, enabling novel phase discovery and the prediction of self-assembly behavior in block copolymer systems with unprecedented efficiency.[17–24] For example, Xuan et al.[17,18] trained ML models to predict the effective Hamiltonian and saddle points of the density fields obtained from SCFT simulations in the AF framework, which accelerates the computational exploration of design parameter space for block copolymers. Chen and Dorfman[19] leveraged a deep convolutional generative adversarial network to propose new initial fields for SCFT calculations that enable de novo phase discovery. Nakamura[20] developed a neural network model with a theory-embedded layer to predict the phase behavior of polymeric solutions. Various neural network-based solvers[21,22] have also been developed to tackle the partial differential equations in SCFT.

In this work, we leverage deep neural networks to accelerate simulations based on the DE-AF field theory framework. In particular, we investigate analytically and numerically partial saddle

point solutions of the auxiliary fields for different representative density fields. Subsequently, utilizing knowledge gained from this investigation, we develop neural networks with highly efficient local and low-dimensional feature representations, and train these networks using simulation data of one-dimensional phases to predict partial saddle points, which can then be used to initialize new SCFT simulations. Interestingly, we find that new simulations initialized from these ML generated guesses find converged solutions for partial saddle points much faster than those started from random initial field configurations for large-cell simulations with a high spatial resolution, even though the data we use to train the ML models was obtained at much lower resolution. Our ML model and results could serve as blueprints for the accelerated computational prediction of the self-assembly behavior of heterogeneous polymers.

II. PARTIAL SADDLE POINTS OF INSTANTANEOUS DENSITY FIELDS

A. Saddle-point density fields

In the DE-AF framework, when the instantaneous density fields are also saddle points $\phi^*(\mathbf{r})$ of the density fields, i.e.,

$$\left.\frac{\delta H[\phi, w_A, w_B]}{\delta \phi(\mathbf{r})}\right|_{\phi^*} = 0, \tag{13}$$

the partial saddle points $w_A^*[\phi]$ and $w_B^*[\phi]$ are saddle points of the Hamiltonian $H[\phi, w_A, w_B]$ for a simulation box with a *fixed* shape and volume, i.e., they coincide with SCFT solutions. Plugging Eq. 2 into Eq. 13, one arrives at the following relationship:

$$i[w_A^*(\mathbf{r}) - w_B^*(\mathbf{r})] = \chi N[1 - 2\phi^*(\mathbf{r})]. \tag{14}$$

Interestingly, this is a *local linear* relationship, i.e., the difference $w_A^* - w_B^*$ in the auxiliary fields at a given spatial grid point $\mathbf{r}$ is only related to the density field ϕ at that spatial grid point. We note that Eq. 13 is analogous to the SCFT saddle point condition in the AF framework,[25] except that here the auxiliary fields $w_A^*(\mathbf{r})$ and $w_B^*(\mathbf{r})$ are purely imaginary while the corresponding saddle point auxiliary fields in the AF framework can be either real or pure imaginary depending on the sign of the eigenvalue of the exchange normal mode. Recently, it has been found that SCFT equations in the AF framework admit additional complex-valued saddle points,[25] but here we focus on physically meaningful solutions – restricting attention to saddle points with real-valued density fields and purely imaginary $w_A^*(\mathbf{r})$ and $w_B^*(\mathbf{r})$. In addition, if $w_A^*[\phi]$ and $w_B^*[\phi]$ are partial

saddle points for a given $\phi(\mathbf{r})$, then adding a constant to either $w_A^*[\phi]$ or $w_B^*[\phi]$ preserves the partial saddle point condition. This implies a nonuniqueness in the solutions for $w_A^*[\phi]$ or $w_B^*[\phi]$. In this work, to eliminate this trivial degeneracy, we set

$$\int d\mathbf{r}\, w_A^*(\mathbf{r}) = \int d\mathbf{r}\, w_B^*(\mathbf{r}) = 0. \tag{15}$$

Under this normalization, we have

$$i[w_A^*(\mathbf{r}) - w_B^*(\mathbf{r})] = 2\chi N[f - \phi^*(\mathbf{r})], \tag{16}$$

where f is the spatially averaged volume fraction of the A block.

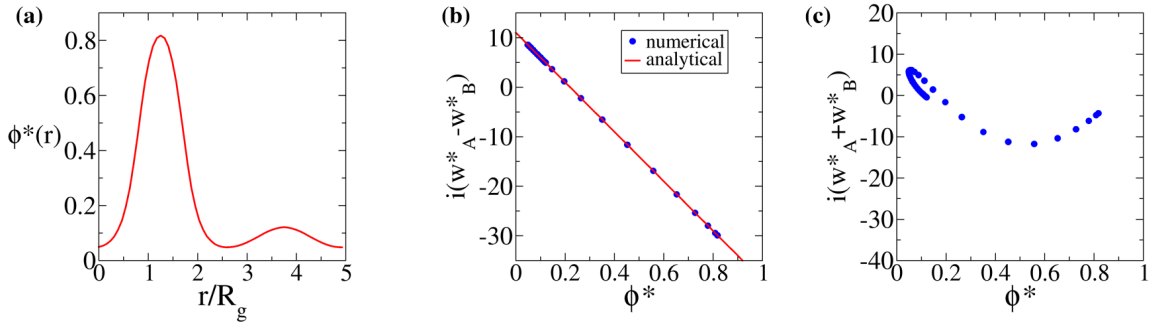

FIG. 1. The saddle point density profile $\phi^*(\mathbf{r})$ (a) solved by the auxiliary field SCFT simulation at $\chi N = 25$, $f = 0.22$ and $L = 5.0R_g$, and the corresponding converged $iw_A^*[\phi^*] - iw_B^*[\phi^*]$ (b) and $iw_A^*[\phi^*] + iw_B^*[\phi^*]$ (c) fields in the DE-AF simulation. The analytical expression given in Eq. 16 that links $iw_A^*[\phi^*] - iw_B^*[\phi^*]$ to $\phi^*(\mathbf{r})$ is shown in (b) to compare to simulation.

As a representative example, we ran one-dimensional auxiliary-field SCFT simulations at $\chi N = 25$, $f = 0.22$ and box length $L = 5.0R_g$. The simulations were subject to periodic boundary conditions and the converged saddle point field $\phi^*(\mathbf{r})$ is shown in Fig. 1(a), which is a (defective) layered structure with a large primary peak and a small secondary peak in the real-space density profile. Subsequently, we use this converged $\phi^*(\mathbf{r})$ as the target density profile in the DE-AF framework and numerically obtain the corresponding $w_A^*[\phi^*]$ and $w_B^*[\phi^*]$. Indeed, Fig. 1(b) shows $iw_A^* - iw_B^*$ against the values of ϕ^*, exhibiting quantitative agreement with the analytical expression given in Eq. 16, provided that the difference between consecutive field iterates (i.e., field error tolerance) is set to 10^{-8}. In contrast, a field error tolerance of 10^{-5} is deemed sufficient for the

thermodynamic properties of interest. For instance, this level of tolerance yields an error in the Hamiltonian of order $10^{-7}k_BT$ per chain in the DE-AF simulation. On the other hand, the dependence of $iw_A^* + iw_B^*$ on $\phi^*(\mathbf{r})$ is highly nonlocal and nonlinear, and can involve a multi-valued mapping, i.e., a given value of ϕ^* could correspond to multiple values of $iw_A^* + iw_B^*$, as shown in Fig. 1(c). This relationship is strongly influenced by the specific shape of $\phi^*(\mathbf{r})$.

B. Non-saddle point density fields

For density fields $\phi(\mathbf{r})$ that are not saddle points of H, Eq. 16 no longer holds, and the $w_A^*[\phi](\mathbf{r})$ and $w_B^*[\phi](\mathbf{r})$ fields are related to $\phi(\mathbf{r})$ in a nonlinear, nonlocal way as mentioned above. Here, we investigate numerically the relationships in these cases of non-saddle point $\phi(\mathbf{r})$. In particular, we consider non-saddle point $\phi(\mathbf{r})$ generated by a type of single-mode reciprocal-space perturbation. Specifically, we start from a saddle-point $\phi^*(\mathbf{r})$, and generate a non-saddle point $\phi(\mathbf{r})$ by randomly varying the values of the Fourier transform $\hat{\phi}^*(\mathbf{q})$ of $\phi^*(\mathbf{r})$ for wave vectors $\mathbf{q}$ in a shell around the location $\mathbf{q}^*$ of the principal wave vector with a thickness δ, i.e.,

$$\hat{\phi}(\mathbf{q}) = \gamma\hat{\phi}^*(\mathbf{q}) \quad \text{for } ||\mathbf{q}| - |\mathbf{q}^*|| < \delta. \tag{17}$$

To make sure that $\phi(\mathbf{r})$ is real-valued, we set γ to be the same for any pair of $\mathbf{q}$ and $-\mathbf{q}$ that satisfy the above equation. For 1D small-cell simulations, we choose a sufficiently small δ such that the density profile is perturbed only at a single pair of $\mathbf{q}$ and $-\mathbf{q}$. To ensure that $\phi(\mathbf{r})$ is between 0 and 1 at each spatial grid point (so that it is physical and consistent with the incompressible melt condition), we sample the random coefficient γ from a uniform distribution in the range of [0.90, 1.0], i.e., $\gamma \sim U[0.90, 1.0]$. We use this range of γ close to 1 since we intend to focus on structures that are well microphase-separated, and also avoid situations where the simulations fail to find numerical solutions for the partial saddle points or converge very slowly.

Figure 2 shows an example of a non-saddle point $\phi(\mathbf{r})$ at $\chi N = 25$, $f = 0.22$ and $L = 3.0R_g$ obtained by this type of perturbation of the corresponding saddle point. This example illustrates that the specific type of perturbation that we consider essentially drives the system towards a more homogeneous state with slightly damped peak and valley in 1D. In Fig. 3 we present the numerically solved partial saddle points $w_A^*[\phi] - w_B^*[\phi]$ and $w_A^*[\phi] + w_B^*[\phi]$. The $iw_A^* - iw_B^*$ difference field is no longer a linear functional of $\phi(\mathbf{r})$; in particular, the nonlinearity is evident deep inside the B-rich region ($\phi \approx 0$).

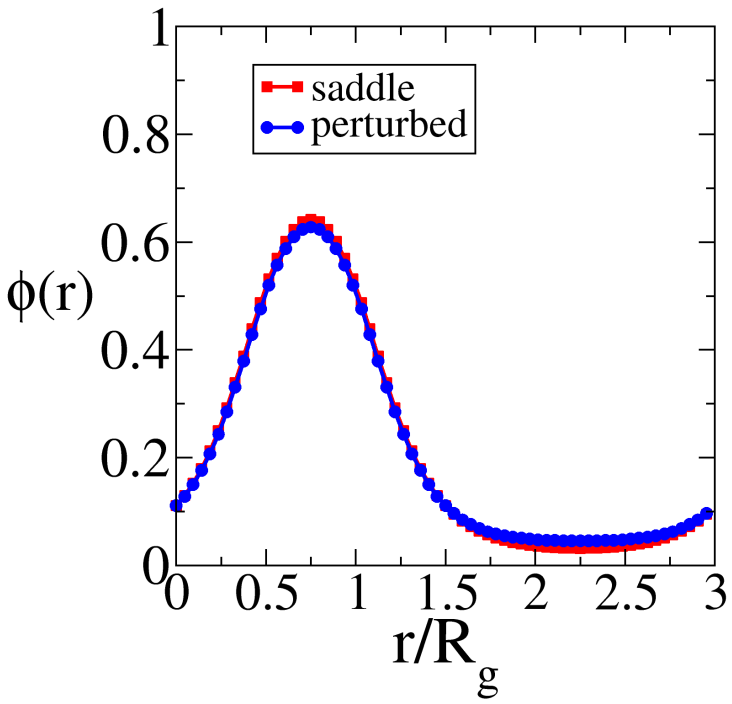

FIG. 2. A representative example of a non-saddle point $\phi(\mathbf{r})$ obtained by single-mode reciprocal-space perturbation of a saddle point at $\chi N = 25$, $f = 0.22$ and $L = 3.0R_g$.

C. Effect of domain spacing

To model an infinite or very large system in the bulk using a finite-size simulation box, computer simulations typically rely on periodic boundary conditions. System size and (in 2D or 3D) shape effects are particularly important in SCFT simulations of copolymer mesophases, which respond elastically as they are distorted away from their preferred equilibrium pattern.[2] The implication is that a saddle point configuration $\phi^*(\mathbf{r})$ at a given cell shape and volume will no longer be the saddle-point solution at another cell shape and volume. Specifically, in one dimension, the domain length of the box affects the partial saddle points w_A^* and w_B^*. As shown in Fig. 4, as one increases the box length L from 3.0 R_g to 3.2 R_g at $\chi N = 25$ and $f = 0.22$ (i.e., stretches the distance between adjacent grid points without changing the magnitudes of ϕ at each grid point), the saddle point $\phi^*(\mathbf{r})$ at $L = 3.0R_g$ is no longer a saddle point at $L = 3.2R_g$, and the solution of $iw_A^* - iw_B^*$ deviates slightly from the analytical form given by Eq. 16. Here we apply a small variation of L to

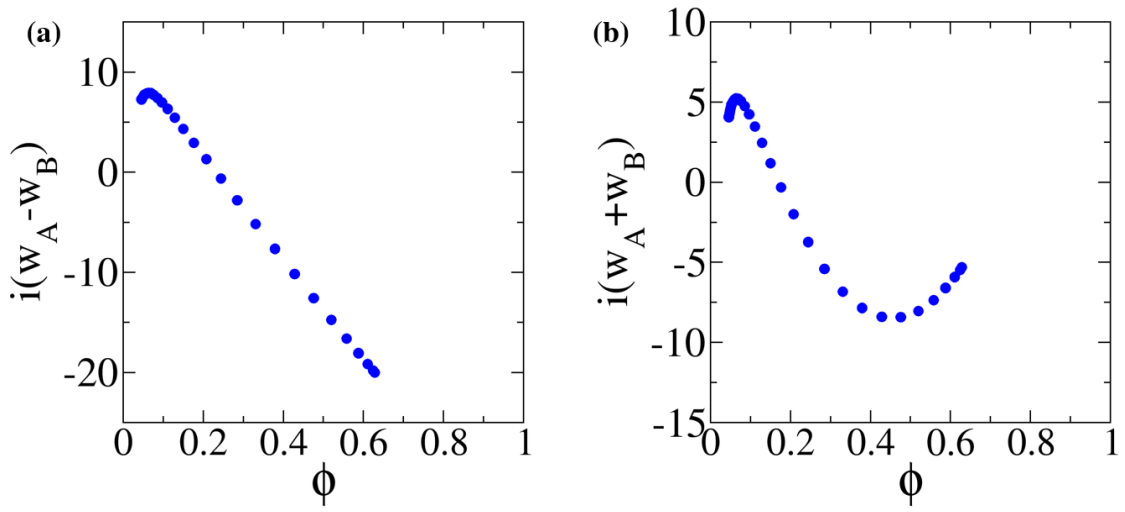

FIG. 3. Partial saddle points $w_A^*[\phi] - w_B^*[\phi]$ and $w_A^*[\phi] + w_B^*[\phi]$ for the non-saddle point $\phi(\mathbf{r})$ at $\chi N = 25$, $f = 0.22$ and $L = 3.0R_g$ in Fig. 2 from simulation.

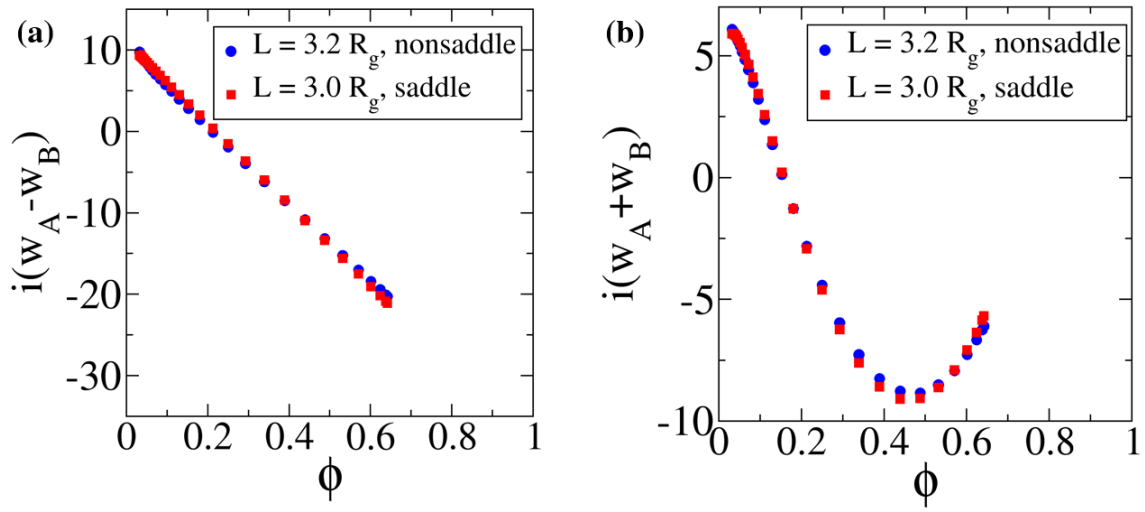

FIG. 4. Partial saddle points $w_A^*[\phi] - w_B^*[\phi]$ and $w_A^*[\phi] + w_B^*[\phi]$ for the non-saddle point $\phi(\mathbf{r})$ obtained by stretching the box of a saddle point $\phi(\mathbf{r})$ from $L = 3.0R_g$ to 3.2 R_g at $\chi N = 25$, $f = 0.22$, along with the partial saddle points at $L = 3.0R_g$.

avoid situations where the simulations fail to find numerical solutions for partial saddle points or

converge very slowly.

III. ML MODEL

Utilizing the insights obtained from analyzing the solutions of partial saddle points, we now design and train neural networks to accelerate DE-AF field-theoretic simulations under the PSPA assumption. We describe in this section the feature selection, model architecture, and data collection process for our ML model.

A. Local representation and model architecture

Recently, neural networks using local frame descriptors as features[26,27]—which describe the local environments around atoms—have been very successful in advancing deep potential molecular dynamics. Here, we follow a similar path and use a local density representation for our ML model in the context of field-based simulations. Specifically, we learn a local mapping from the local *scalar* ϕ, the magnitude of its gradient $|\nabla\phi|$ and its Laplacian $\nabla^2\phi$ at a given spatial grid point (and other global features) to the scalar values of w_A and w_B at that grid point. The inclusion of $\nabla^2\phi$ is motivated by the appearance of $\nabla^2 q$ in the governing equation for the chain propagator $q(\mathbf{r}, s; [iw_A, iw_B])$, which is connected to the volume fraction operator $\tilde{\phi}_A(\mathbf{r})$. This operator is constrained to match $\phi(\mathbf{r})$ under the partial saddle point condition. Regarding global features, it is well known that for conformationally symmetric AB linear diblock copolymers, the equilibrium phase behavior at the mean-field level is dictated by the volume fraction f of the A block and segregation strength χN at the mean field level.[2] Therefore, we incorporate χN and f as input features. Additionally, we incorporate ϕ_{max} and ϕ_{min}, representing the maximum and minimum values of the density profile, respectively. These features provide the model with global context about the profile, compensating for the fact that predictions are made independently at each spatial grid point. Furthermore, we select the principal wavenumber q^*—the wavenumber at which the structure factor $S(k)$ reaches its maximum—as a feature to encode information about the natural scale of the self-assembly, which is related to the cell shape and volume in the case of small-cell simulations.

This local mapping offers several advantages: it is independent of the specific copolymer mesophase, applicable across different spatial dimensions and resolutions, and invariant under

translations and rotations of polymer species density fields. Moreover, generating the data required to learn this mapping is much less costly than learning a full mapping from a given *scalar field* $\phi(\mathbf{r})$ to the $w_A(\mathbf{r})$ and $w_B(\mathbf{r})$ fields in a simulation box with a given shape and volume. For instance, a single simulation of a 1D phase with a spatial resolution of 64 produces 64 samples under this local density representation, whereas it yields only one sample for a full mapping. Also, due to the low-dimensional nature of the feature space, training a ML model is much easier compared to using a feature representation based on the scalar field $\phi(\mathbf{r})$.

Given the complex nature of the mapping between the input features and the $w_A(\mathbf{r})$ and $w_B(\mathbf{r})$ fields, here we employ a feedforward deep neural network with fully connected layers to learn this mapping. We treat the number of hidden layers (i.e., depth of the neural network) and the number of neurons in each hidden layer (i.e., width of the neural network) as hyperparameters to tune. Considering the analytical relationship given by Eq. 16 for the saddle-point density $\phi(\mathbf{r})$, the neural network is trained to learn $u_- = i[w_A^*(\mathbf{r}) - w_B^*(\mathbf{r})] - 2\chi N[f - \phi(\mathbf{r})]$ and $u_+ = i[w_A^*(\mathbf{r}) + w_B^*(\mathbf{r})]$. The form of u_- is related to the saddle-point condition in Eq. 16 corresponds to the residual terms in the fields $w_A(\mathbf{r})$ and $w_B(\mathbf{r})$ fields and is reminiscent of the approach used in another recent ML study.[17] We use the mean squared error between the predicted values u_+ and u_- and their corresponding ground truth values $\tilde{u}+$ and $\tilde{u}-$ (obtained from DE-AF SCFT simulations) as the loss function $\mathscr{L}$. Specifically,

$$\mathscr{L} = \frac{1}{2N_s}[\sum_{j=1}^{N_s}(u_{j,-} - \tilde{u}_{j,-})^2 + \sum_{j=1}^{N_s}(u_{j,+} - \tilde{u}_{j,+})^2], \tag{18}$$

where the index j runs over all samples, and N_s denotes the total number of samples. The Continuously Differentiable Exponential Linear Unit (CELU)[28] is used as the nonlinear activation function for all hidden layers, which produces the following output $\sigma(z)$ for a given input z:

$$\sigma(z) = \begin{cases} z, & z \geq 0, \\ \alpha[\exp(z/\alpha) - 1], & z < 0. \end{cases} \tag{19}$$

Here, we set the parameter $\alpha = 1$ for all hidden units. We find that CELU outperforms the widely used Rectified Linear Unit (ReLU) in our task, likely due to CELU's smooth gradients and ability to mitigate neuron inactivity. The model architecture of our neural network is schematically shown in Fig. 5.

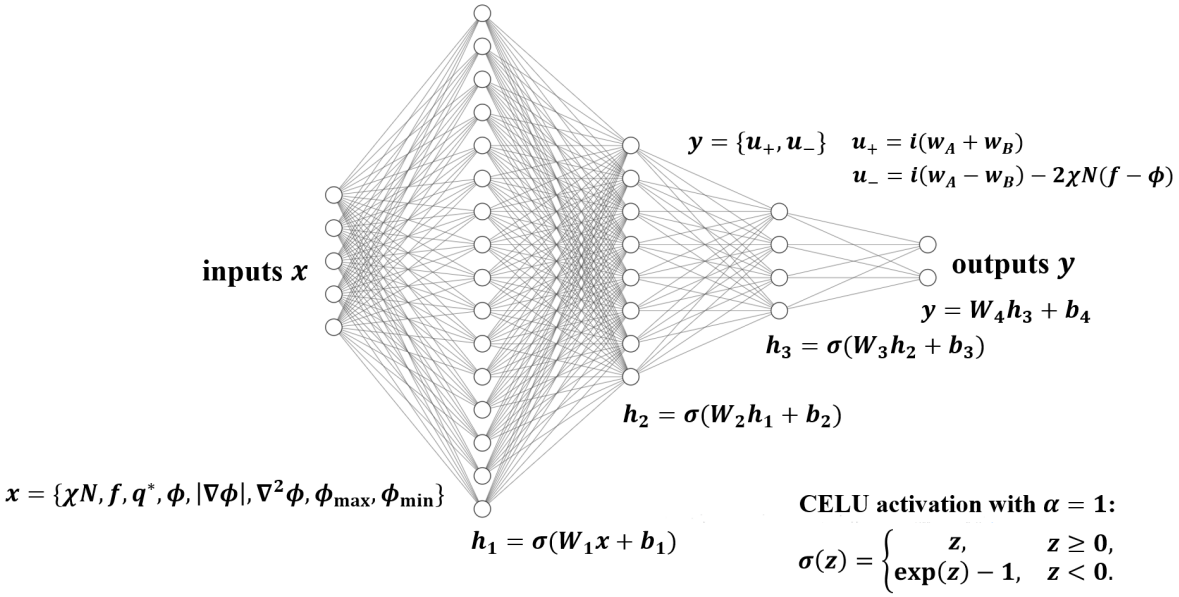

FIG. 5. Illustration of the model architecture for our deep neural networks with an efficient local density feature representation $(\chi N, f, q^*, \phi, |\nabla\phi|, \nabla^2\phi, \phi_{\max}, \phi_{\min})$.

B. Data collection

To generate the data for training and evaluating the neural network, we performed SCFT simulations with a fixed simulation box to obtain 1D saddle point density profiles for 160 microstructures with a spatial resolution of 64, covering the parameter ranges $\chi N \in \{25, 30, 35, 40\}$, $f \in \{0.22, 0.26, 0.30, 0.34, 0.38, 0.42, 0.46, 0.50\}$, and $L/R_g \in \{3.0, 3.5, 4.0, 4.5, 5.0\}$. We use these small-cell simulations to better resolve the structures at a given spatial resolution of 64. To incorporate non-saddle point cases into our dataset, we apply the previously described single-mode reciprocal-space perturbation to each saddle point density profile, generating 8 independent non-saddle point profiles per saddle point. To further displace the profiles from the saddle point, we also perturb the parameters χN and L according to $(\chi N)' = \gamma_1 \chi N$ and $L' = \gamma_2 L$ for these non-saddle points, where $\gamma_1 \sim U[0.95, 1.05]$ and $\gamma_2 \sim U[0.95, 1.05]$. Here we choose small perturbations for χN and L to avoid situations where the simulations fail to find numerical solutions for partial saddle points or converge very slowly. In total, we have collected 160+160×8=1440 density profiles with a spatial resolution of 64, which correspond to 1440×64=92160 samples due to the local density representation we are using. We set the field error tolerance to 10^{-8} for all simulations

when generating the data set to ensure high data quality.

Subsequently, following standard practice, we randomly partition the collected data into three sets: a training set consisting of 1008 density profiles (or 64512 samples), a cross validation set consisting of 216 density profiles (or 13824 samples), and a test set consisting of 216 density profiles (or 13824 samples). The training set is used to learn the neural network parameters (weights and biases), the cross-validation set is used to tune hyperparameters, and the test set is used to assess the performance of the trained network on previously unseen data.

IV. DATA-DRIVEN PREDICTION FOR PARTIAL SADDLE POINTS

A. ML model performance

We employ the Adaptive Moment Estimation (i.e., Adam) Optimizer[29] to train the aforementioned neural networks shown in Fig. 5 using the training set. The learning rate and weight decay of the Adam optimizer, along with the number of hidden layers and neurons per layer in the neural network, are treated as hyperparameters and tuned using the cross-validation set. Initially, we employed a simpler ML model using $(\chi N, f, q^*, \phi, |\nabla\phi|)$ as input features, but found that these features alone do not provide sufficient information to accurately predict partial saddle points. As a result, we incorporated the previously mentioned features $\nabla^2\phi, \phi_{\max}, \phi_{\min}$ into the feature set. The neural network was trained for 20000 epochs with a batch size of 128, and the best model was recorded that yields the lowest loss on the cross validation set after the first 10000 epochs. We were able to achieve a cross-validation loss $\mathscr{L}$ as low as 0.04 using a neural network with three hidden layers containing 80, 40, and 16 neurons, respectively, and a learning rate of 5.0×10^{-4} and a weight decay of 1.0×10^{-5}, as shown by the learning curves in Fig. 6. This performance underscores the value of including $\nabla^2\phi$, $\phi_{\max}$, and $\phi_{\min}$ as input features, which enrich the model with both local and global information about the density field and make up for the fact that we are using ML models that decouple different spatial grid points when making the predictions.

The performance of the trained ML model was evaluated by making predictions on the test set that was never seen by the model during training or hyperparameter tuning. The loss $\mathscr{L}$ was found to be 0.03 for the test set, indicating that our model generalizes well to new, unseen data. In particular, we show in Fig. 7(a) the predicted partial saddle point of $w_A^*[\phi] - w_B^*[\phi]$ and $w_A^*[\phi] + w_B^*[\phi]$ alongside the one obtained from DE-AF field theory simulation (treated as ground

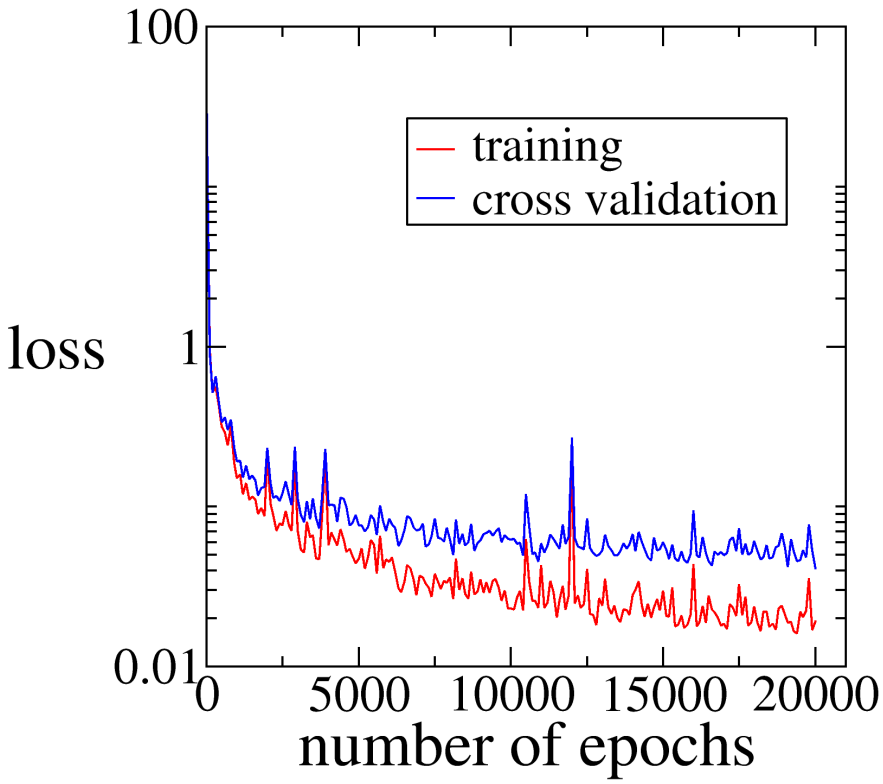

FIG. 6. Training and cross validation loss as functions of the number of epochs for the optimized neural network with three hidden layers containing 80, 40, and 16 neurons, respectively, trained using a batch size of 128, a learning rate of 5.0×10^{-4} and a weight decay of 1.0×10^{-5}.

truth) for the saddle point of $\phi(\mathbf{r})$ at $\chi N = 30$, $f = 0.26$, and $L = 5.0R_g$. The field $w_A^*[\phi] - w_B^*[\phi]$ again is a linear functional of ϕ, which is well captured by the ML model. In Fig. 7(b) the predicted and true partial saddle point of $w_A^*[\phi] - w_B^*[\phi]$ and $w_A^*[\phi] + w_B^*[\phi]$ at $\chi N = 34.6859$, $f = 0.50$, and $L = 4.9836R_g$ for a non-saddle point density profile is shown, which again indicates good agreement between ML model prediction and simulation. In Fig. 7(c), we show the predicted and true partial saddle points for the density profile on which the ML model performs the worst—specifically, at $\chi N = 38.6934$, $f = 0.42$, and $L = 2.9074R_g$. This data point lies at the boundary of the ranges of χN and L covered by our dataset. Nonetheless, the agreement is reasonably good even for this case, except for a few grid points deep inside the A-rich or B-rich region.

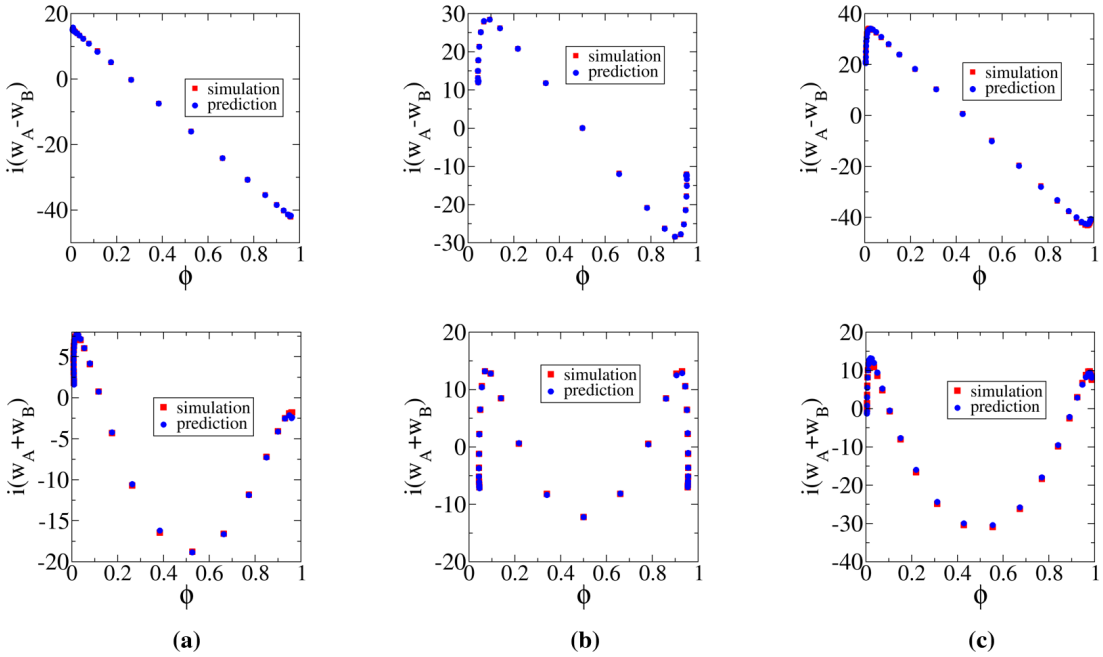

FIG. 7. Partial saddle points of $w_A^*[\phi] - w_B^*[\phi]$ (top row) and $w_A^*[\phi] + w_B^*[\phi]$ (bottom row) predicted by ML model (blue) and from DE-AF field theory simulation (red) for different density profiles. (a) A saddle-point density profile at at $\chi N = 30$, $f = 0.26$, and $L = 5.0R_g$. (b) A non-saddle point density profile at $\chi N = 34.6859$, $f = 0.50$, and $L = 4.9836R_g$. (c) A non-saddle point density profile at $\chi N = 38.6934$, $f = 0.42$, and $L = 2.9074R_g$.

B. Generalization to higher spatial dimension

Since the local density representation in our ML model is universal across spatial dimensions, we can make predictions for partial saddle points in higher dimensions even though the model is trained only on 1D simulation data. As an example, Fig. 8 shows a three dimensional non-saddle point density profile generated by perturbing the body-centered cubic phase that is a saddle point at $\chi N = 35$, $f = 0.30$, and $L = 4.5R_g$, and the machine learned prediction of the partial saddle points of $iw_A^*(\mathbf{r}) - iw_B^*(\mathbf{r})$ and $iw_A^*(\mathbf{r}) + iw_B^*(\mathbf{r})$ along with the corresponding converged solutions from simulation (treated as ground truth). The agreement between the ML prediction and the simulation is reasonably good; we expect the agreement to further improve after higher-dimensional simulation data are added to the training and tuning of the ML model. In this sense, this ML modeling scheme could serve as a building block for future models with superior predictive capabilities.

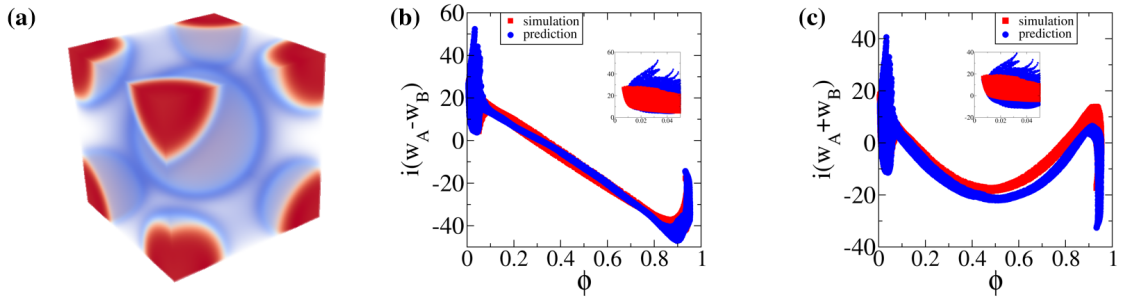

FIG. 8. Visualization of a three dimensional non-saddle point density profile (a) generated by perturbing the body-centered cubic phase that is a saddle point at $\chi N = 35$, $f = 0.30$, and $L = 4.5R_g$, and the machine learned prediction (blue) of the partial saddle points of $iw_A^*(\mathbf{r}) - iw_B^*(\mathbf{r})$ (b) and $iw_A^*(\mathbf{r}) + iw_B^*(\mathbf{r})$ (c) along with the corresponding converged solutions from simulation (red). The insets in (b) and (c) show the regions near $\phi = 0$.

C. Acceleration of density-explicit simulations at high spatial resolution

All the density profiles in the training, cross validation, and test set employed were 1D profiles with a spatial resolution of 64. However, due to the fact that the local density representation in the ML model decouples different spatial grid points and treats them separately, we can easily make predictions for partial saddle points at other resolutions as well. As a proof of concept, we generate quenched saddle point density profiles with a spatial resolution of 2048 using large-cell AF SCFT simulations for two examples where we allow the cell length to vary to obtain stress-free configurations (i.e., variable-cell approach[2]): the first at $\chi N = 30$ and $f = 0.40$, and the second at $\chi N = 34$ and $f = 0.37$. The cell lengths in these two cases are equilibrated to $205.19R_g$ and $210.82R_g$, respectively. We then apply a single-mode reciprocal space perturbation to obtain one non-saddle point density profile $\phi(\mathbf{r})$ from each of these two saddle-point density profiles, as shown in the left column of Fig. 9(a) and (b), respectively. The two resulting non-saddle point density profiles are then used as target profiles in DE-AF simulations, with two types of initializations: one from a random field and the other from the ML model prediction. A field error tolerance of 10^{-5} was applied for these DE-AF simulations. The ML predicted partial saddle points for the $iw_A^*(\mathbf{r})$ and $iw_B^*(\mathbf{r})$ fields appear to be close to the converged ones in simulations (middle and right column of Fig. 9, respectively). Consequently, we observe a 3.9× and 2.0× improvement in convergence speed

when the simulations are initialized with the ML predictions compared to random initialization in these two cases, respectively. In the second case, the converged $iw_A^*(\mathbf{r})$ and $iw_B^*(\mathbf{r})$ fields possess greater variation in local peak intensities compared to the first case. This increased variation likely necessitated more fine tuning of the field solutions in later stages of the simulations, contributing to the reduced speedup provided by machine learned initialization. Nonetheless, overall these two cases demonstrate the utility of the model in accelerating simulations beyond the conditions of the data it is trained on.

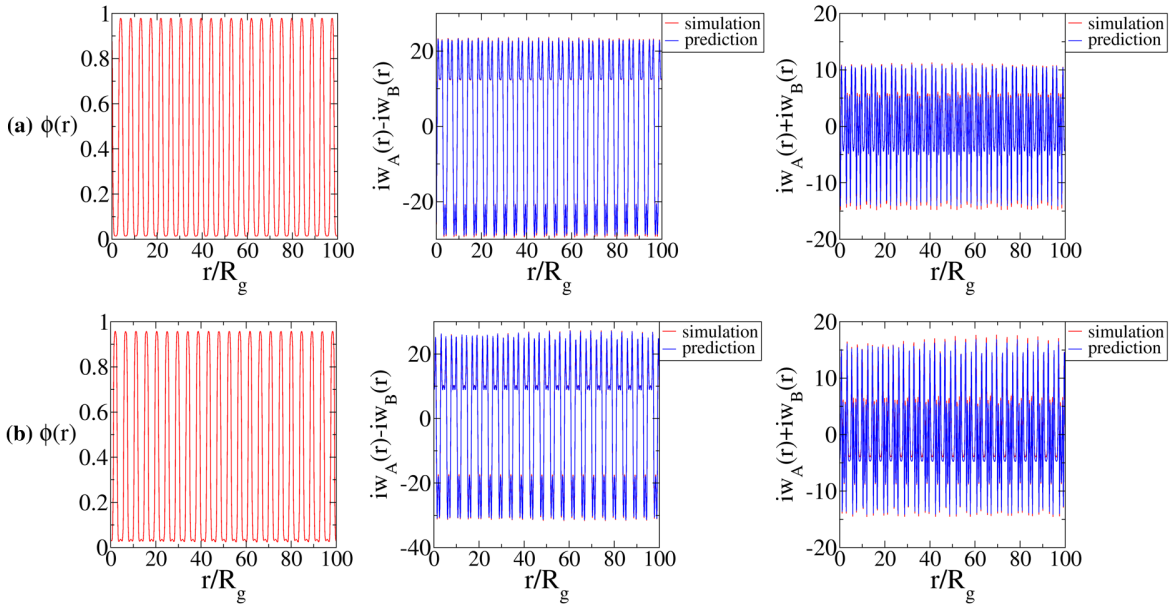

FIG. 9. Non-saddle point density profiles $\phi(\mathbf{r})$ (left column) at a high spatial resolution of 2048 and the corresponding partial saddle points $iw_A^*(\mathbf{r})$ (middle column) and $iw_B^*(\mathbf{r})$ (right column) predicted by the ML model (blue) and from simulations (red) for two conditions: (a) $\chi N = 30$, $f = 0.40$, and $205.19R_g$. (b) $\chi N = 34$, $f = 0.37$, and $210.82R_g$. Here we only show a portion of the boxes for better visual clarity.

V. CONCLUSIONS AND DISCUSSION

In this work, we analytically and numerically investigated the partial saddle points of the auxiliary fields corresponding to various density profiles—both those that are saddle points of H and those that are not—in the DE-AF framework of polymer field theory, using a linear diblock

copolymer system as an example, and examined factors that affect the solutions of these partial saddle points. This initial study motivated the development of a ML model utilizing an efficient local density feature representation that is applicable across different spatial dimensions and resolutions, and invariant under translations and rotations of the polymer species density fields. We integrated this representation into deep neural networks and trained the models on 1D simulation data with a spatial resolution of 64 to accurately predict the partial saddle points of the auxiliary fields under varying conditions. Remarkably, the machine-learned model produces high-quality initial guesses that considerably accelerated new simulations—even at resolutions as high as 2048, far exceeding the resolution of the training data. The model was also seen to make resonable predictions of partial saddle points for 3D structures, even though all the training data was restricted to 1D. Overall, our ML framework could form the basis for new ML-assisted field simulation tools enabling the computational study of various polymer and other soft-matter systems, including multi-species/multi-component systems.

It is noteworthy that our trained ML models can be easily incorporated into existing field simulation tools since they only involve matrix multiplications and simple nonlinear transformations, and the parameters such as the weights W and biases b in the neural networks can be input into the simulation tools just like initial field configurations. Strictly speaking, the ML model accelerates only the solution of partial saddle points of the auxiliary fields at fixed density profiles, which is the inner loop in the DE-AF framework. Although the outer loop that evolves the density profiles remains the same, the overall DE-AF field theory simulation is accelerated. This could be particularly useful for dynamic SCFT simulations that are computationally expensive due to the inner loop. Moreover, even with just the inner loop, we can directly determine the energetics of different instantaneous density profiles, e.g. those inferred from experiments, which could be a potentially useful tool on its own.

In addition, we note that here we are invoking the partial saddle point approximation, and given a density profile the algorithm seeks one scalar auxiliary field for each species in the system. Therefore, when making predictions for the partial saddle points, we can employ standard feed-forward deep neural networks, which are relatively simple deep ML models. Alternatively, if one wants to accelerate fully fluctuating, density-explicit field-theoretic simulations (FTS), where in the inner loop one is sampling a *distribution* of field configurations for each species auxiliary field, there are more advanced deep learning models such as diffusion models[30] that are well suited for such a task.

ACKNOWLEDGMENTS

This work was supported by the U.S. Department of Energy, Office of Basic Energy Sciences, under Award Number DE-SC0019001. H. D. C. acknowledges partial support by the National Science Foundation under Award Number DMS-2410252. Use was made of computational facilities purchased with funds from the National Science Foundation (OAC-1925717 and CNS-1725797) and administered by the Center for Scientific Computing (CSC). The CSC is supported by the California NanoSystems Institute and the Materials Research Science and Engineering Center (MRSEC; NSF DMR-2308708) at UC Santa Barbara. The research reported here made use of shared facilities of the UC Santa Barbara MRSEC (NSF DMR-2308708), a member of the Materials Research Facilities Network (www.mrfn.org) and the BioPACIFIC Materials Innovation Platform of the National Science Foundation under Award No. DMR-1933487.

REFERENCES

[1]G. H. Fredrickson, V. Ganesan, and F. Drolet, "Field-theoretic computer simulation methods for polymers and complex fluids," Macromolecules **35**, 16–39 (2002).

[2]G. H. Fredrickson, *The equilibrium theory of inhomogeneous polymers*, 134 (Oxford University Press: Oxford, 2006).

[3]K. T. Delaney and G. H. Fredrickson, "Recent developments in fully fluctuating field-theoretic simulations of polymer melts and solutions," J. Phys. Chem. B **120**, 7615–7634 (2016).

[4]M. W. Matsen, "Field theoretic approach for block polymer melts: SCFT and FTS," J. Chem. Phys. **152** (2020).

[5]S. F. Edwards, "The statistical mechanics of polymers with excluded volume," Proc. Phys. Soc. **85**, 613 (1965).

[6]G. H. Fredrickson and K. T. Delaney, *Field Theoretic Simulations in Soft Matter and Quantum Fluids*, Vol. 173 (Oxford University Press, 2023).

[7]J. Hubbard, "Calculation of partition functions," Phys. Rev. Lett. **3**, 77 (1959).

[8]A. Weyman, V. G. Mavrantzas, and H. C. Öttinger, "Field-theoretic simulations beyond δ-interactions: Overcoming the inverse potential problem in auxiliary field models," J. Chem. Phys. **155** (2021).

[9]A. Weyman, V. G. Mavrantzas, and H. C. Öttinger, "Direct calculation of the functional inverse

of realistic interatomic potentials in field-theoretic simulations," J. Chem. Phys. **156** (2022).

[10]T. Quah, K. T. Delaney, and G. H. Fredrickson, "Preserving positivity in density-explicit field-theoretic simulations," J. Chem. Phys. **161** (2024).

[11]M. Müller and F. Schmid, "Incorporating fluctuations and dynamics in self-consistent field theories for polymer blends," Advanced Computer Simulation Approaches for Soft Matter Sciences II , 1–58 (2005).

[12]J. G. E. M. Fraaije, "Dynamic density functional theory for microphase separation kinetics of block copolymer melts," J. Chem. Phys. **99**, 9202–9212 (1993).

[13]J. G. E. M. Fraaije, B. A. C. Van Vlimmeren, N. M. Maurits, M. Postma, O. A. Evers, C. Hoffmann, P. Altevogt, and G. Goldbeck-Wood, "The dynamic mean-field density functional method and its application to the mesoscopic dynamics of quenched block copolymer melts," J. Chem. Phys. **106**, 4260–4269 (1997).

[14]C. Yeung and A.-C. Shi, "Formation of interfaces in incompatible polymer blends: A dynamical mean field study," Macromolecules **32**, 3637–3642 (1999).

[15]R. Hasegawa and M. Doi, "Adsorption dynamics. extension of self-consistent field theory to dynamical problems," Macromolecules **30**, 3086–3089 (1997).

[16]T. Quah, C. Balzer, K. T. Delaney, and G. H. Fredrickson, "Efficient dynamical field-theoretic simulations for multi-component systems," J. Chem. Phys. **162** (2025).

[17]Y. Xuan, K. T. Delaney, H. D. Ceniceros, and G. H. Fredrickson, "Deep learning and self-consistent field theory: A path towards accelerating polymer phase discovery," J. Comput. Phys. **443**, 110519 (2021).

[18]Y. Xuan, K. T. Delaney, H. D. Ceniceros, and G. H. Fredrickson, "Machine learning and polymer self-consistent field theory in two spatial dimensions," J. Chem. Phys. **158** (2023).

[19]P. Chen and K. D. Dorfman, "Gaming self-consistent field theory: Generative block polymer phase discovery," Proc. Natl. Acad. Sci. U.S.A. **120**, e2308698120 (2023).

[20]I. Nakamura, "Phase diagrams of polymer-containing liquid mixtures with a theory-embedded neural network," New J. Phys. **22**, 015001 (2020).

[21]Q. Wei, Y. Jiang, and J. Z. Y. Chen, "Machine-learning solver for modified diffusion equations," Phys. Rev. E **98**, 053304 (2018).

[22]D. Lin and H.-Y. Yu, "Deep learning and inverse discovery of polymer self-consistent field theory inspired by physics-informed neural networks," Phys. Rev. E **106**, 014503 (2022).

[23]S. Zhao, T. Cai, L. Zhang, W. Li, and J. Lin, "Autonomous construction of phase diagrams of

block copolymers by theory-assisted active machine learning," ACS Macro Lett. **10**, 598–602 (2021).

[24]D. Yong and J. U. Kim, "Accelerating langevin field-theoretic simulation of polymers with deep learning," Macromolecules **55**, 6505–6515 (2022).

[25]W. Kang, D. Yong, and J. U. Kim, "Characteristics of the complex saddle point of polymer field theory," Macromolecules **57**, 3850–3861 (2024).

[26]L. Zhang, J. Han, H. Wang, R. Car, and W. E, "Deep potential molecular dynamics: a scalable model with the accuracy of quantum mechanics," Phys. Rev. Lett. **120**, 143001 (2018).

[27]J. Zeng, D. Zhang, D. Lu, P. Mo, Z. Li, Y. Chen, M. Rynik, L. Huang, Z. Li, S. Shi, *et al.*, "Deepmd-kit v2: A software package for deep potential models," J. Chem. Phys. **159** (2023).

[28]J. T. Barron, "Continuously differentiable exponential linear units," arXiv preprint arXiv:1704.07483 (2017).

[29]D. P. Kingma, "Adam: A method for stochastic optimization," arXiv preprint arXiv:1412.6980 (2014).

[30]D. E. Habibi, G. Aarts, L. Wang, and K. Zhou, "Diffusion models learn distributions generated by complex langevin dynamics," arXiv preprint arXiv:2412.01919 (2024).